A Texture-Polarization Method for Estimating Convective/Stratiform Precipitation Area Coverage from Passive Microwave Radiometer Data

William S. Olson[1], Ye Hong[2], Christian D. Kummerow[3], and Joseph Turk[4]

[1]JCET/University of Maryland Baltimore County

[2]The Aerospace Corporation, Los Angeles, California

[3]Department of Atmospheric Sciences, Colorado State University, Fort Collins, Colorado

[4]Naval Research Laboratory, Monterey, California

(Submitted to the *Journal of Applied Meteorology*)

August 21, 2000

Abstract

Observational and modeling studies have described the relationships between convective/stratiform rain proportion and the vertical distributions of vertical motion, latent heating, and moistening in mesoscale convective systems. Therefore, remote sensing techniques which can quantify the relative areal proportion of convective and stratiform rainfall can provide useful information regarding the dynamic and thermodynamic processes in these systems. In the present study, two methods for deducing the convective/stratiform areal extent of precipitation from satellite passive microwave radiometer measurements are combined to yield an improved method. If sufficient microwave scattering by ice-phase precipitating hydrometeors is detected, the method relies mainly on the degree of polarization in oblique-view, 85.5 GHz radiances to estimate the area fraction of convective rain within the radiometer footprint. In situations where ice scattering is minimal, the method draws mostly on texture information in radiometer imagery at lower microwave frequencies to estimate the convective area fraction.

Based upon observations of 10 convective systems over ocean and 9 systems over land, instantaneous, 0.5° resolution estimates of convective area fraction from the Tropical Rainfall Measuring Mission Microwave Imager (TRMM TMI) are compared to nearly coincident estimates from the TRMM Precipitation Radar (TRMM PR). The TMI convective area fraction estimates are slightly low-biased with respect to the PR, with TMI-PR correlations of 0.78 and 0.84 over ocean and land backgrounds, respectively. TMI monthly-average convective area percentages in the tropics and subtropics from February 1998 exhibit the greatest values along the ITCZ and in continental regions of the summer (southern) hemisphere. Although convective area percentages from the TMI are systematically lower than those from the PR, monthly rain patterns derived from the TMI and PR rain algorithms are very similar. TMI rain depths are significantly higher than corresponding rain depths from the PR in the ITCZ, but are similar in magnitude elsewhere.

Introduction

Understanding the complex interaction of convective cloud systems and their environment has been a major objective of meteorological research for many years. The vertical transports of sensible heat, moisture, and momentum by clouds have a direct impact on environmental flow fields, while larger-scale radiative and dynamical processes can change the stability characteristics of the atmosphere, thereby enhancing or suppressing convective activity. The larger-scale flow can also determine the organization of convection and the nature of the vertical transports by convective-scale motions.

In numerical weather prediction models and general circulation models, which currently have grid resolutions on the order of 100 km, convective processes are highly parameterized, and the accuracy of simulations based upon these models depends upon an adequate representation of cloud effects at sub-grid scale. A description of the mesoscale organization of convective systems requires relatively high grid-resolution in numerical models, and even if such models are available it is unclear whether or not the effects of organization on storm-scale transports can be properly simulated.

Over the last half-century, several field campaigns have provided data needed for a better understanding of convective systems and their effects. These campaigns have focussed observations from surface instruments, rawinsondes, radar, and aircraft sensors over regions spanning areas ~100,000 km^2 and periods up to several months in order to gather information pertaining to the microphysics, kinematics, organization, and environmental impact of convective systems. Although much has been learned from these campaigns, a more large-scale, long-term perspective can be gained through the use of satellite remote sensing of cloud properties, especially over oceanic regions where long-term monitoring by other methods is generally unfeasible. Such observations could be used to track climatological variations in

convective organization and transports, and provide a means of validating cloud properties and effects simulated by numerical prediction models.

The capability of satellite passive microwave sensors to provide quantitative precipitation estimates is now well established (ref. Ebert et al. 1996; Smith et al. 1998). Passive microwave rain estimates are possible because there is a fairly direct physical relationship between the path-integrated water content of rain along the sensor line of sight and the upwelling radiances measured by the sensor at frequencies less than about 40 GHz. Passive microwave observations can be used to infer other cloud/precipitation properties such as ice-phase precipitation amount, and they may be employed to describe the organization of convective systems. However, these uses of the data have received much less attention.

Regarding organization, the basic structure of a convective system can be described by the proportion and distribution of convective and stratiform rainfall within the system (Houze 1989). Previous observational and modeling studies have established the relationships between convective/stratiform rain proportion and the vertical distributions of vertical motion, latent heating, and moistening in convective systems (e.g. Houze 1989; Sui et al. 1997; Tao et al. 1993). Therefore, microwave remote sensing techniques that yield the proportions of convective and stratiform rainfall within a sensor footprint may ultimately provide useful information regarding the dynamic and thermodynamic processes in these systems.

In the present study, two methods for determining the areal proportion of convective and stratiform precipitation within a footprint of the TRMM Microwave Imager (TMI) are combined to yield an improved technique that emphasizes the strengths of both methods. In Section 2, the two methods and their merger are described. Applications of the combined method to TMI observations of individual convective systems are presented in Section 3, including statistics of intercomparisons with convective area estimates from the TRMM Precipitation Radar (PR).

Monthly estimates of convective area proportion over the tropics from both TMI and PR are presented in Section 4. A summary and discussion are included in Section 5.

2. Methods

a. Texture-based Convective/Stratiform Area Fraction

It is commonly known (Zipser 1977; Leary and Houze 1979; and Houze 1993) that stratiform precipitation regions are associated with the relatively weak updrafts or downdrafts while convective regions are associated with more vigorous, turbulent updrafts. According to mass continuity arguments, a change in vertical velocity must be associated with change in the horizontal mass field. Thus, it is assumed that the substantial horizontal gradients of precipitation (and likewise microwave radiances) are indicative of convective regions. The texture-based method empirically relates the horizontal structure of radiances to the convective area fraction within the TMI footprint.

Based on data from the TOGA COARE, Hong et al. (1999) tested several indices, derived from passive microwave radiance measurements, for separating convective and stratiform rain areas. In that study a convective/stratiform index (CSI) was developed that combined the local maximum variation of radiance and magnitude of radiance from the 19 GHz, 37 GHz, and 85.5 GHz horizontal-polarization channels. Formally,

$$CSI_c = VM_{37h} + 0.5 \cdot VM_{19h} + 0.25 \cdot \left(TB_{19h} - TB_{19h-clear}\right), \tag{1}$$

$$CSI_s = VM_{85h} + \left(TB_{85h-clear} - TB_{85h}\right), \tag{2}$$

and

$$CSI = \left(1 - w_s\right) \cdot CSI_c + w_s \cdot CSI_s. \tag{3}$$

Here, TB_{vp} and $TB_{vp\text{-clear}}$ are the microwave radiance and "background" clear-air radiance, respectively, at frequency v and polarization p. The variable VM_{vp} is the local maximum variation with respect to any of the neighboring measurements. At 85.5 GHz, the local maximum variation is defined as

$$VM_{85h} = \begin{cases} \max_j \left(TB_{85h,j} - TB_{85h} \right), \text{ if greater than 0} \\ 0, \text{ otherwise,} \end{cases} \tag{4}$$

while at 19.35 and 37.0 GHz, the local maximum variation is

$$VM_{vp} = \begin{cases} \max_j \left(TB_{vp} - TB_{vp,j} \right), \text{ if greater than 0} \\ 0, \text{ otherwise.} \end{cases} \tag{5}$$

In (4) and (5), the subscript j refers to any of the eight neighboring footprints surrounding the footprint being analyzed. The local maximum variation is used here because the relatively low resolution of the microwave radiance observations may smear emission or scattering gradients in any particular direction.

Since convection is generally associated with heavy precipitation, the differential magnitude of the radiance with respect to the background radiance is added to the CSI [third term on the right-hand side of (1) and second term on the right-hand side of (2)]. The addition of the differential magnitude of the radiance to the CSI_e and CSI_s also minimizes the sensitivity of maximum variation to data quality. Determination of the background clear-air radiances is described in Hong et al. (1999). The final index, CSI, is a weighted sum of the emission and

scattering indices; the weighting factor w_s increases with the relative amount of scattering in the microwave footprint.

$$w_s = \begin{cases} 0, & TB_{85h} > TB_{85h-clear} \\ \left(TB_{85h-clear} - TB_{85h}\right)/80\,\mathrm{K}, & TB_{85h-clear} - 80\,\mathrm{K} < TB_{85h} < TB_{85h-clear} \\ 1, & TB_{85h} < TB_{85h-clear} - 80\,\mathrm{K}. \end{cases} \quad (6)$$

Therefore, the variability of the 85.5 GHz ice-scattering signature mainly determines *CSI* when significant ice is present, whereas the variability of emission at both 19.35 and 37.0 GHz mainly determine *CSI* when little ice is present.

Hong et al. (1999) demonstrated that mixed convective/stratiform rainfall areas and fluxes increase gradually as resolution degrades. Over a 6 km x 6 km area, which is about the size of the TMI's highest resolution footprints, the contribution to the total rain flux by mixed regions (here defined as regions where convective rain covers 30 – 70% of the total area) was about 30%, based upon an analysis of TOGA COARE shipboard radar data. The contribution from mixed precipitation increases to about 50% over 12 km x 12 km areas, comparable to the footprint area of the highest-resolution SSM/I channels. Therefore, instead of classifying a TMI footprint as either convective or stratiform, these authors related the index (3) to the area fraction of convective rainfall within a footprint by matching the cumulative distributions of convective area fractions derived from COARE shipboard radar data and synthesized TMI *CSI* measurements. This probability matching approach was utilized since any small spatial misregistration of the two datasets could lead to low correlations between the convective area fraction and *CSI*. The resulting empirical relationship is well-approximated by

$$f_{CSI} = \begin{cases} 0, & CSI < 30\,\mathrm{K} \\ \left\{1.333\times10^{-2}\cdot(CSI - 30\,\mathrm{K}), & 30\,\mathrm{K} \le CSI \le 105\,\mathrm{K} \\ 1, & \mathrm{CSI} > 105\,\mathrm{K}. \end{cases} \quad (7)$$

Readers are referred to Hong et al. (1999) for a more detailed description of the texture-based convective/stratiform separation algorithm.

b. Polarization-based Convective/Stratiform Area Fraction

An alternative formula for convective area fraction is suggested by the analyses of SSM/I observations by Spencer et al. (1989) and Heymsfield and Fulton (1994a,b). These authors found significant differences, on the order of 5 K or greater, between the vertically- and horizontally-polarized 85.5 GHz radiances in stratiform rain regions over land, whereas regions of strong convection were nearly unpolarized at 85.5 GHz. Although the physical basis of these polarization differences has not been verified, the aforementioned authors hypothesized that precipitation-sized ice particles such as snow or aggregates would tend to become oriented as they fall through the relatively weak updrafts or downdrafts of stratiform rain regions, resulting in preferential scattering in the horizontal polarization. The more vigorous, turbulent updrafts of convective regions would cause ice hydrometeors to lose any preferred orientation, leading to similar scattering signatures in both polarizations.

More recently, Turk and Vivekanandan (1995), Petty and Turk (1996), and Schols et al. (1997) performed microwave radiative transfer calculations through clouds of oriented, aspherical ice hydrometeors and found polarization differences exceeding 5 K, supporting the earlier hypothesis. In Olson et al. (1999) the approximately inverse relationship between 85.5 GHz polarization difference and convective fraction was utilized to constrain retrievals of precipitation and latent heating from Special Sensor Microwave Imager (SSM/I) observations. In the present study, a somewhat different analysis of 85.5 GHz polarization data is utilized to infer the convective area fraction within the TMI footprint.

A plot of the TMI observed 85.5 GHz polarization difference versus the average of the 85.5 GHz radiances is presented in Fig. 1. These observations are derived TMI overpasses of 10

organized convective systems over ocean (Fig. 1a) and 9 convective systems over land (Fig. 1b), sampled from the first two years of the TRMM mission. Overlaid on these observations are radiative transfer model simulated 85.5 GHz polarization differences and average radiances for atmospheres containing layers of rain, cloud, and ice precipitation. The model atmosphere is characterized by tropical profiles of temperature and water vapor, and a layer of non-precipitating cloud liquid water with a water content of 0.5 g m^{-3} is assumed between 1 and 6 km altitude. Embedded in this atmosphere is a uniform rain layer between the surface and 4 km, in which the equivalent rain rate is varied from 0 to 50 mm h^{-1}. For each rain rate, the thickness of a capping graupel layer is varied between 0 and 8 km, and the equivalent water content of graupel within the layer is assumed to be equal to the rain water content. Raindrops are assumed to be oblate spheroidal, with the oblateness increasing with drop equivalent volume diameter. Graupel particles are conical in shape, with a constant density of 0.6 g cm^{-3}. Both rain and graupel are oriented such that the long axes of the particles are parallel to the earth's surface. Calculations of the upwelling radiances at 53.4° incidence (close to the 52.8° incidence angle of the TMI) are performed using a polarized multistream radiative transfer method (Evans and Stephens, 1991). Since the earth's surface is entirely obscured by the rain-free model atmosphere at 85.5 GHz, only over-ocean radiative calculations are considered in the intercomparisons of Fig 1. Details of the radiative modeling can be found in Turk and Vivekenandan (1995) and Petty and Turk (1996).

Note first in Fig. 1a the relatively large polarization differences greater than 20 K that are characteristic of the observed cloud-free regions over the ocean. These polarization differences are due to the highly polarized emission from the ocean surface that is only partially absorbed by water vapor in a clear atmosphere. Clouds in the atmosphere strongly absorb the polarized surface emission, and thermal emission from these particles raises the observed upwelling radiances at 85.5 GHz. The transition from cloud-free to cloudy atmospheres creates the nearly

vertical branch of datapoints corresponding to average 85.5 GHz radiances greater than 230 K in Fig. 1a.

A cloud liquid water path exceeding 2.5 kg m^{-2} renders the cloudy atmosphere almost completely absorbing, and nearly unpolarized blackbody cloud emission close to the cloud-top temperature at the freezing level (273 K) is observed. This limit is confirmed by the radiative transfer model calculations, which indicate a maximum average radiance of 272.5 K with a 0.1 K polarization difference for an atmosphere containing only non-precipitating cloud.

In precipitating clouds, weak microwave scattering by raindrops and strong scattering by precipitation-sized ice particles reduces the upwelling radiance by diverting the upwelling emission from lower levels. Note the congregation of observations along an approximate 45° diagonal line in Fig. 1a, indicating increasing 85.5 GHz polarization difference with decreasing average 85.5 GHz radiance. These observations generally correspond to stratiform areas in mesoscale convective systems. An empirical linear fit to these "purely stratiform" observations is indicated in the figure. Also in Fig. 1a, the radiative transfer model simulations incorporating oriented ice hydrometeors exhibit a similar trend, with polarization generally increasing with decreasing average radiance. As the scattering by ice precipitation becomes very strong, with radiances falling below 160 K, the polarization at 85.5 GHz levels off and then decreases. The TMI observations suggest that these modeled combinations of very low average radiances and large polarization differences do not occur naturally, likely because the large concentrations of ice precipitation required can only be supported by strong, convective updrafts.

By contrast, radiative transfer simulations based upon atmospheres containing randomly oriented ice particles yield nearly unpolarized radiances at 85.5 GHz (ref. Haferman, 2000). This limiting case is represented by the zero-polarization "purely convective" line in Fig. 1a. If it is assumed that the TMI footprints at 85.5 GHz are essentially filled with precipitation, but contain different proportions of convective and stratiform rain, then a combination of the strongly

polarized "purely stratiform" model radiances and the nearly unpolarized "purely convective" model radiances within each TMI footprint could explain the scatter of observed 85.5 GHz polarization differences and average radiances that fall between these limits. The clustering of observations near the "purely stratiform" model curve is due to the greater frequency of occurrence of stratiform rain that also tends to fill the TMI 85.5 GHz footprints. Smaller-scale convective elements occur less frequently and are often mixed with stratiform rain within the sensor's field of view.

It is evident from Fig. 1b that over land, the polarization of 85.5 GHz radiances in rain-free areas is quite low, but the relationship between polarization differences and average 85.5 GHz radiances in precipitating areas is similar to that observed over ocean.

If it is assumed that TMI 85.5 GHz polarization differences in purely convective regions are essentially zero, and that they follow a quasi-linear relationship with average 85.5 GHz radiances in stratiform regions, then an estimate of the convective area fraction within the sensor footprint is given by

$$f_{POL} = \begin{cases} 0, & POL > POL_{strat} \\ 1 - \dfrac{POL}{POL_{strat}}, & POL_{strat} \geq POL \geq 0 \\ 1, & POL < 0, \end{cases} \tag{8}$$

where

$$POL = TB_{85v} - TB_{85h}, \tag{9}$$

and

$$POL_{strat} = a \cdot \left[\frac{TB_{85v} + TB_{85h}}{2} \right] + b. \tag{10}$$

In the empirical linear relationship relating the polarization difference to the average 85.5 GHz radiance in stratiform regions, the constants a (-0.192) and b (52.4 K) have been adjusted to obtain a best fit with the cluster of TMI observations. Here the broad assumption is that the footprint is completely filled with rain, such that the polarized (nearly unpolarized) emission from the ocean (land) background does not contribute significantly to the total observed radiance. Given the oblique viewing angle of the TMI (52.8° angle of incidence) and the relatively small footprint of the 85.5 GHz channels (4 km x 7 km), this is not too unreasonable an assumption.

c. Merger of Techniques

Figs. 2 and 3 illustrate the strengths and weakness of the texture-based (f_{CSI}) and polarization-based (f_{POL}) methods for estimating the area fraction of convection within a TMI footprint. In Fig. 2, a tropical convective system near the Cape Verde Islands is observed by the TMI, and the texture- and polarization-based convective fractions are displayed in Fig. 2a and 2b, respectively.

For comparison, TMI-observed 85.5 GHz radiances are shown in Fig. 2c, and area fractions of convection based upon TRMM Precipitation Radar (PR) data using the algorithm of Awaka et al. (1998) are presented in Fig. 2d. The Awaka algorithm distinguishes convective and stratiform rain regions by examining the texture of the higher-resolution PR reflectivity data in both the vertical and horizontal directions. The vertical PR profile is examined to determine whether or not a bright band of reflectivity, normally associated with stratiform precipitation, is present. In the horizontal, the reflectivities in adjacent PR footprints are analyzed using a modified version of the method of Steiner et al. (1995) to identify convective centers. The vertical and horizontal analyses are combined to classify each PR footprint as convective, stratiform, or indeterminate. Since the PR data resolve precipitation spatial structure at a higher

vertical resolution (0.25 km) and horizontal resolution (4.4 km) than the TMI data, the PR convective/stratiform classification is considered to be a reliable reference in the present study.

In order to more directly compare the relatively high resolution PR convective/stratiform classification to convective area fraction estimates from the TMI, a weighted average of the PR-classified footprints in the neighborhood of a given TMI footprint is performed. Following Hong et al. (1999), a PR convective area fraction is defined by

$$f_{PR} = \sum_j g_j \cdot PRcs_j \Big/ \sum_j g_j , \tag{11}$$

where

$$PRcs_j = \begin{cases} 1, & \text{convective PR classification} \\ 0, & \text{otherwise} \end{cases} \tag{12}$$

is based upon the Awaka et al. (1998) PR classification, and

$$g_j = \exp\left[-\ln(2)\, r_j^2 / r_0^2\right] \tag{13}$$

is a gaussian weighting factor. Here, r_j is the distance in km between a PR footprint, indexed by j, and the specified TMI footprint, and the summation in (11) is over all PR footprints within $2.5r_0$ of the TMI footprint. A value of r_0 equal to 3.5 km leads to a PR convective area fraction estimate that is comparable in resolution to the TMI estimate.

In Fig. 2, note that in regions of strong scattering at 85.5 GHz (radiance depressions in Fig. 2c), both the texure- and polarization-based TMI methods identify the convective bands

associated with the tropical system, as depicted in the PR classification (Fig. 2d). However, the weaker bands near 15N, 28W, and near 14N, 30W produce less ice scattering, and these are more clearly depicted by the texture-based method. In this case, local maxima of emission at 19.35 and 37 GHz [see (1)] help to identify these bands, whereas the polarization of the weakly scattered radiances provides little information.

The imagery of Fig. 3 is from an overpass of Hurricane Floyd in the western Atlantic on September 13, 1999. In the PR classification of Fig. 3d, convection in the eyewall of Floyd forms a complete ring around the eye near 24N, 71W. The ring has a slightly greater width on the northwest side of the eyewall. Both the texture- and polarization-based methods in Fig. 3a and b, respectively, indicate convection surrounding the eye, with a greater convective fractions on the northwest side of the eyewall. The hurricane rainbands to the east of the eye are strongly patched with convection in the PR classification, while the bands to the west are dominated by stratiform precipitation. This spatial variation is also seen in the polarization-based estimates of convective fraction; however, the texture-based method shows more limited convection to the east and some weak but extended convective bands to the west. It appears that the texture-based method is responsive to the intensity and spatial variations of 85.5 GHz scattering signatures (see Fig. 3c) that do not always correspond to the presence of convection. Here, the polarization-based method provides a more realistic overall depiction of the distribution of convection in Floyd, although noise and scan-to-scan gain jumps in the TMI 85.5 GHz data lead to some artifacts.

To take advantage of the relative strengths of the texture- and polarization-based methods for estimating convective area fraction, the estimates from each method are combined in inverse proportion to the expected error variance of each at a given location. This is the minimum variance estimate as described by Daley (1991). An estimate of the error variance of the texture-based convective fraction is based upon intercomparisons of TMI-based convective fractions and

coincident ground-based radar observations from TOGA COARE. These intercomparisons indicate greater uncertainty in convective fraction estimates when there is a mixture of convective and stratiform precipitation within the radiometer footprint, whereas in the middle of largely convective or stratiform regions, the uncertainty is less. An empirical fit to the error variance of the convective area fraction as a function of *CSI* is given by

$$var_{CSI} = v_0 + v_1 \cdot CSI + v_2 \cdot CSI^2, \tag{14}$$

where v_0, v_1, and v_2 are 0.246653, 6.667 x 10^{-3}, and –4.762 x 10^{-5}, respectively.

The error of the polarization-based convective fraction estimate is primarily a function of the 85.5 GHz scattering depression. For a very small scattering depression, the expected polarization difference in stratiform rain areas becomes very small, and by (8), the error variance of the convective fraction estimate is inversely proportional to the square of the "stratiform" polarization.

$$var_{POL} = \frac{\left[2\,POL_{strat}^2 + \left\{(a \cdot POL)^2/2\right\}\right] \cdot var_{TB85}}{POL_{strat}^4} + \mathrm{var}_f \tag{15}$$

Here, var_{TB85} is the variance of noise in the TMI 85.5 GHz radiance measurements (assumed to be 1 K^2), and var_f is the error variance in the estimate of area convective fraction from the polarization method in the absence of noise (estimated to be 0.1) .

The combined estimate of convective area fraction within a TMI footprint is given by

$$f_{COM} = \frac{(f_{CSI}/var_{CSI}) + (f_{POL}/var_{POL})}{(1/var_{CSI}) + (1/var_{POL})}. \tag{16}$$

d. Modification for Over-Land Applications

In applications of the convective area fraction method over land or coastal regions, the interpretation of CSI_e is ambiguous, since local variations of emission are usually indistinguishable from the relatively strong background surface emission. Therefore, although (13) is formally applied over all surfaces, over land and coastal regions the weight w_s in (6) is set equal to 1; i.e., the texture-based convective area fraction estimate is only a function of the scattering index, CSI_s.

3. Applications to TRMM TMI Observations

a. Signatures of Convective Area Fraction in TMI Observations

Prior to performing direct comparisons of the TMI merged algorithm convective area fraction against similar estimates from the PR, the scattering and polarization signatures of convective area fraction are examined. Plotted in Fig. 4a and b are the PR mean convective area fractions corresponding to pairs of 85.5 GHz average radiance (abscissa) and polarization difference (ordinate) over ocean and land backgrounds, respectively. The plots are derived from the same sets of TMI observations shown in Fig. 1a and b, which have been collocated with nearly coincident PR observations. For comparison, the "purely stratiform" and "purely convective" lines from the polarization-based convective area fraction method are superimposed on the data.

Note that there is a clear trend of increasing convective area fraction, deduced from the PR, with distance perpendicular to the "purely stratiform" line of the polarization-based method over either background. However, over land there is also a trend of increasing convective area fraction with decreasing average 85.5 GHz radiance for values of convective fraction greater than 0.5. These two trends suggest that the relationship between convective area fraction and 85.5 GHz radiance is indeed more complex than the graphical polarization-based technique

represented by (8), and that the quantification of the 85.5 GHz scattering signature in (2) should help to improve estimates of convective area fraction.

b. TMI-PR Convective Area Fraction Intercomparisons

In Fig. 5, applications of the combined texture-polarization method for convective area fraction, (16), to TMI observations of precipitation systems over ocean (right panels) are compared to nearly coincident PR convective fraction estimates (left panels) from (11). In general, there is a fairly reasonable correlation between convective fraction estimates in the relatively large-scale convective bands. Due to the higher resolution and finer sampling of the PR, smaller-scale convective features and isolated convective elements are sometimes detected by the PR and not by the TMI. For example, convection near 17.5N, 139.5E in panel 5b, and near 26N, 91W in panel 5f is identified using the PR method, but convection in the corresponding TMI images is either weak or non-existent.

The TMI and PR convective area fractions over land in Fig. 6 are also reasonably correlated, even though information from the texture of microwave emission signatures (1) is not available in the combined texture-polarization TMI method. The lack of emission information may not be as critical a factor over land, where there is a greater probability that precipitation-sized ice particles are produced in convective regions due to generally greater atmospheric instability and stronger updrafts. Also for this reason, isolated convection may be more easily detected by the TMI over land; e.g., convective cells near 1N, 67W in Fig. 6c and 6d. Over both ocean and land, noise and gain jumps in the 85.5 GHz observations can lead to false convective signatures in the TMI method. For example, the TMI falsely identifies convection along a scan line near 33N, 83W in Fig. 6a, where no convection is found in the PR data (Fig 6b).

Collocated TMI and PR convective area fraction estimates from the 10 convective systems over ocean and 9 convective systems over land (see Figs. 1 and 4) are plotted in Fig. 7a and 7b,

respectively. Note that these estimates are spatially averaged over 0.5° x 0.5° boxes to minimize data geolocation errors. Bivariate statistics of the collocated, box-averaged estimates are presented in Table 1. Although there is scatter in the plotted estimates either over ocean or land, there is also an obvious correlation between the estimates. The correlation coefficient between the TMI and PR estimates is 0.78 over oceanic regions and 0.84 over land backgrounds. The TMI convective fraction estimates are systematically lower than the PR estimates, with a bias of –0.02 over ocean or land. The standard deviation of the differences between the TMI and PR estimates are 0.06 and 0.07 over ocean and land, respectively. Note that these statistics are somewhat skewed by the relatively large number of low convective fraction estimates. For example, based upon the PR algorithm the mean convective fraction over ocean is only 0.05. From Fig. 7, it appears that both the bias and standard deviation of differences increase with increasing convective area fraction.

4. Monthly-Mean Estimates of Convective Area Proportion

In addition to instantaneous TMI-PR comparisons, large-scale distributions of convective area fraction are compared for the month of February, 1988. Instantaneous, convective area fraction estimates from the TMI and PR are averaged in 5° x 5° boxes over the month. Note that these convective fraction estimates represent the ratio of the convective area to the *total* area observed by the sensors, rather than the ratio of the convective area to the raining area. This definition enables a direct comparison of convective area estimates without ambiguities introduced by differing estimates of the raining area from TMI and PR. The distributions of mean convective area percentage from the TMI and PR are displayed in the first two panels of Fig. 8. For comparison, monthly rain depths derived from the TRMM operational TMI (2A-12) and PR (3A-25) algorithms are shown in the third and fourth panels, respectively. Only TMI convective fraction and rain estimates from footprints located within the PR swath contribute to the TMI convective percentages and rain depths in Fig. 8.

TMI convective area percentages are greatest in the Inter-Tropical Convergence Zone (ITCZ) and over the continental regions in the summer (southern) hemisphere. The South Pacific Convergence Zone, Gulf of Mexico and midlatitude storm track regions of the western Atlantic and western Pacific Oceans also exhibit significant values.

PR convective area percentages (second panel of Fig. 8) are generally greater than the TMI estimates, although the patterns of convective coverage are similar. At a given location, the PR convective area percentage is typically 0.5% greater than the corresponding TMI convective percentage; see scatterplot in Fig. 9. The most noticeable differences occur over the winter (northern) hemisphere oceans, where PR convective percentages often exceed 0.5%, while TMI convective percentages are usually less than 0.5%. One possible explanation for these differences is the greater sensitivity of the PR to isolated convective cells over the ocean (see Section 3b). Isolated convection over the ocean is sometimes not detected by the TMI due to the larger footprints of the instrument and the difficulty of discriminating precipitation polarization signatures from the polarized ocean background.

In spite of the fact that TMI convective percentages are typically less than those derived from the PR, TMI rain depths in the ITCZ are generally greater (third and fourth panels of Fig. 8). In the central Pacific, TMI rain depths are about 50% higher than the corresponding rain depths from the PR. On the other hand, TMI and PR rain depths over the continental regions and in the extra-tropics are very similar in magnitude, and the overall monthly patterns are consistent. The reasons for the differences in TMI and PR rain depths are not obvious: the relationships between rain water content and the observed signatures are very different in the two instruments, and the physical assumptions embodied in the respective algorithms are not the same. However, it appears that the TMI vs. PR differences in retrieved convective area percentages do not show any clear correlation or anti-correlation with differences in retrieved rain depths, and therefore the discrepancies in TMI and PR retrieved rain depths are likely due to other sensor or algorithmic differences.

5. Concluding Remarks

Instantaneous convective area fraction estimates from the Tropical Rainfall Measuring Mission Microwave Imager (TRMM TMI) are compared to nearly coincident estimates from the TRMM Precipitation Radar (TRMM PR) at 0.5° resolution. TMI convective fraction estimates are slightly low-biased with respect to the PR estimates, with correlations of 0.78 and 0.84 over ocean and land backgrounds, respectively. TMI monthly-average convective area percentages in the tropics and subtropics from February 1998 exhibit the greatest values along the ITCZ and in continental regions of the summer (southern) hemisphere. Although convective area percentages from the TMI are systematically lower than those from the PR, monthly rain patterns derived from the TMI and PR rain algorithms are similar. TMI rain depths are significantly higher than corresponding rain depths from the PR in the ITCZ, but are similar in magnitude elsewhere.

One of the admitted weaknesses of the current study is the lack of independent ground validation data for evaluating remote sensing estimates of convective area coverage. The TRMM Ground Validation program will soon produce maps of convective/stratiform rain coverage based upon ground-based radar observations from stations at Melbourne, FL; Houston, TX; Kwajalein, Marshall Islands, and Darwin, Australia. The authors will compare TMI and PR estimates of convective area fraction to the classification data from these sites in a future study; however, the classification of ground-based radar reflectivity data is based upon an analysis of horizontal reflectivity magnitude and texture that may not always reflect the underlying dynamical variations associated with convective/stratiform processes.

Coinciding with a limited number of satellite overpasses are dual-doppler radar observations collected during three of the TRMM field campaigns: the South China Sea Monsoon Experiment, the TRMM Large-scale Biosphere Atmosphere campaign, and the Kwajalein Experiment. Analysis of these dual-doppler observations will yield fields of vertical air motion that should provide a much more definitive convective/stratiform classification. Also, latent

heating vertical structure, which is strongly correlated with vertical air velocity in precipitating clouds, can be estimated by combining dual-doppler vertical velocities with thermodynamic data from coincident radiosonde observations. If agreement between TMI estimates of convective area fraction and the dynamically-consistent, dual-doppler convective/stratiform classification data can be achieved, then the prospects for estimating latent heating distributions from TMI data are much improved.

Acknowledgments: The authors wish to thank Grant Petty and Jeffrey Haferman for helpful discussions regarding the radiative modeling of aspherical ice-phase precipitation, and also Gerald Heymsfield for his insights into the variation of microwave polarization signatures from organized convective systems. This study was funded by the TRMM Science Program.

References

Awaka, J., T. Iguchi, and K. Okamoto, 1998: Early results on rain type classification by the Tropical Rainfall Measuring Mission (TRMM) precipitation radar. Proceedings of the *8th URSI Commission F Open Symp.*, Aveiro, Portugal, 143-146.

Daley, R., 1991: *Atmospheric Data Analysis*. Cambridge University Press, 457 pp.

Ebert, E. E., M. J. Manton, P. A. Arkin, R. J. Allan, G. E. Holpin, and A. Gruber, 1996: Results from the GPCP Algorithm Intercomparison Programme. *Bull. Amer. Met. Soc.*, **77**, 2875-2887.

Evans, K. F., and G. L. Stephens, 1991: A new polarized atmospheric radiative transfer model. *J. Quant. Spectroscopy and Radiative Transfer*, **46**, 413-423.

Haferman, J. L., 2000: Microwave scattering by precipitation. From *Light Scattering by Nonspherical Particles: Theory, Measurements, and Applications*, Academic Press, 690 pp.

Heymsfield, G. M., and R. Fulton, 1994a: Passive microwave and infrared structure of mesoscale convective systems. *Meteorol. Atmos. Phys.*, **54**, 123-139.

Heymsfield, G. M., and R. Fulton, 1994b: Passive microwave structure of severe tornadic storms on 16 November 1987. *Mon. Wea. Rev.*, **122**, 2587-2595.

Hong, Y., C. D. Kummerow, and W. S. Olson, 1999: Separation of convective and stratiform precipitation using microwave brightness temperature. *J. Appl. Meteor.*, **38**, 1195-1213.

Houze, R. A., Jr., 1989: Observed structure of mesoscale convective systems and implications for large-scale heating. *Quart. J. Roy. Meteor. Soc.*, **115**, 425-461.

Houze, R. A., Jr, 1993: *Cloud Dynamics*. Academic Press, 573 pp.

Leary, C. A., and R. A. Houze, Jr., 1979: The structure and evolution of convection in a tropical cloud cluster. *J. Atmos. Sci.*, **36**, 437-457.

Olson, W. S., C. D. Kummerow, Y. Hong, and W.-K. Tao, 1999: Atmospheric latent heating distributions in the Tropics derived from satellite passive microwave radiometer measurements. *J. Appl. Meteor.*, **38**, 633-664.

Petty, G. W., and J. Turk, 1996: Observed multichannel microwave signatures of spatially extensive precipitation in tropical cyclones. Proceedings of the *Eighth Conference on Satellite Meteorology and Oceanography*, Atlanta, GA, Amer. Meteor. Soc., 291-294.

Schols, J., J. Hafermann, J. Weinman, C. Prabhakara, M. Cadeddu, and C. Kummerow, 1997: Proceedings of the *Ninth Conference on Atmospheric Radiation*, Long Beach, CA, Amer. Meteor. Soc., 270-273.

Smith, E. A., J. E. Lamm, R. Adler, J. Alishouse, K. Aonashi, E. Barrett, P. Bauer, W. Berg, A. Chang, R. Ferraro, J. Ferriday, S. Goodman, N. Grody, C. Kidd, D. Kniveton, C. Kummerow, G. Liu, F. Marzano, A. Mugnai, W. Olson, G. Petty, A. Shibata, R. Spencer, F. Wentz, T. Wilheit, and E. Zipser, 1998: Results of the WetNet PIP-2 project. *J. Atmos. Sci.*, **55**, 1483-1536.

Sui, C.-H., K.-M. Lau, Y. N. Takayabu, and D. A. Short, 1997: Diurnal variations in tropical oceanic cumulus convection during TOGA COARE. *J. Atmos. Sci.*, **54**, 639-655.

Spencer, R. W., H. M. Goodman, and R. E. Hood, 1989: Precipitation retrieval over land and ocean with SSM/I: Identification and characteristics of the scattering signal. *J. Atmos. Oceanic Technol.*, **6**, 254-273.

Steiner, M., R. A. Houze, Jr., and S. E. Yuter, 1995: Climatological characterization of three-dimensional storm structure from operational radar and rain gauge data. *J. Appl. Meteor.*, **34**, 1978-2007.

Tao, W.-K., J. Simpson, C.-H. Sui, B. Ferrier, S. Lang, J. Scala, M.-D. Chou, and K. Pickering, 1993: Heating, moisture, and water budgets of tropical and midlatitude squall lines: Comparisons and sensitivity to longwave radiation. *J. Atmos. Sci.*, **50**, 673-690.

Turk, J., and J. Vivekanandan, 1995: Effects of hydrometeor shape and orientation upon passive microwave brightness temperature measurements. *Microwave Radiometry and Remote Sensing of the Environment*, VSP Press, Utrecht, The Netherlands, pp. 187-196.

Zipser, E. J., 1977: Mesoscale and convective-scale downdrafts as distinct components of squall-line circulation. *Mon. Wea. Rev.*, **105**, 1568-1589.

Tables

Table 1. Statistics of collocated, instantaneous 0.5° resolution estimates of convective area fraction from the TRMM Microwave Imager (TMI) and Precipitation Radar (PR) over ocean and land backgrounds. The samples contain 1374 and 823 collocated estimates over ocean and land, respectively.

Background	bias	standard deviation of difference	correlation
Ocean	-0.02	0.06	0.78
Land	-0.02	0.07	0.84

Figure Captions

Fig. 1. Polarization differences plotted versus average 85.5 GHz radiances over (a) ocean and (b) land backgrounds. TMI observations are plotted as points (non-raining areas) and open circles (raining areas). Diamonds represent radiative transfer simulations for atmospheres containing oriented, aspherical liquid and ice-phase precipitation (see text for a detailed description). Dashed lines are approximate curves representing "purely stratiform" and "purely convective" precipitation conditions.

Fig. 2. Imagery of a mesoscale convective system near the Cape Verde Islands in the North Atlantic on 12 September, 1999. Presented in panels (a) and (b) are the convective area fractions within 85.5 GHz footprints based upon TMI texture and polarization information, respectively. TMI 85.5 GHz imagery is presented in (c). PR-derived convective area fractions at a resolution comparable to the TMI are shown in panel (d).

Fig. 3. Same as Fig. 2, but for Hurricane Floyd on 13 September, 1999.

Fig. 4. TMI polarization differences plotted versus average 85.5 GHz radiances over (a) ocean and (b) land backgrounds. The average convective area fraction derived from the PR in TMI 5 K average radiance and 2 K polarization difference intervals is plotted as a different symbol. Dashed lines are approximate curves representing "purely stratiform" and "purely convective" precipitation conditions.

Fig. 5. TMI (left column) and PR (right column) derived convective area fraction estimates for three different convective systems over the ocean. Light shading indicates convective fractions between 0 and 0.3; moderate shading corresponds to convective fractions between 0.3 and 0.7, and dark shading indicates convective fractions between 0.7 and 1.0. Unshaded areas are rain-free or beyond the sensor observing area.

Fig. 6. Same as Fig. 5, but for convective systems over land.

Fig. 7. Scatterplots of coincident, instantaneous convective area fraction estimates at 0.5° resolution from the TMI and PR over (a) ocean and (b) land backgrounds. Solid line indicating "perfect agreement" of estimates is included for reference.

Fig. 8. Monthly-mean estimates of convective area percentage at 5° resolution from the TMI and PR for February, 1998. Note that only TMI convective fraction estimates within the PR swath are included in the monthly average. For comparison, rain depths derived from the TMI (TRMM 2A-12 algorithm) and PR (TRMM 3A-25 algorithm) are shown in the third and fourth panels,

respectively. Again, TMI monthly rain depths are derived only from TMI footprints within the PR swath.

Fig. 9. Scatterplot of 5° resolution, monthly-mean convective fraction estimates from the TMI and PR for February, 1998. Solid line indicating "perfect agreement" of estimates is included for reference.

Fig. 1a

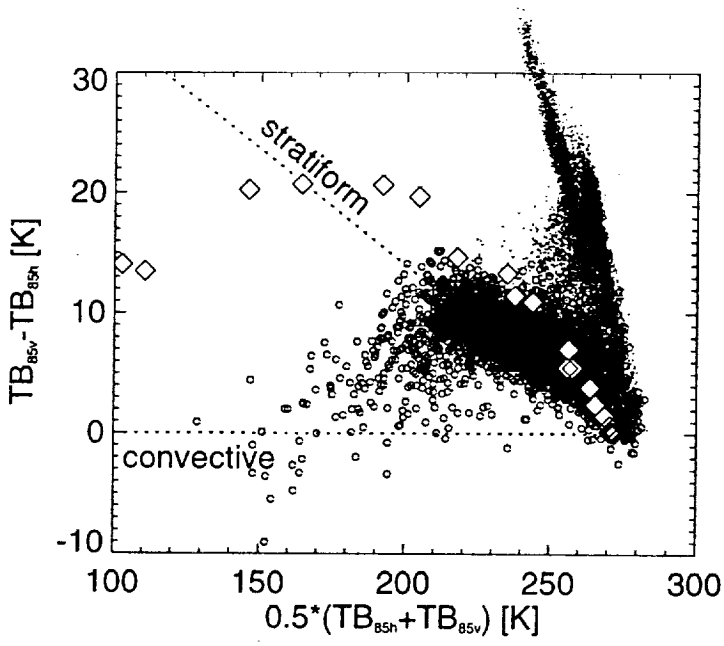
30
20
10
0
-10
100
150
200
250
300
stratiform
convective
TB85v-TB85h [K]
0.5*(TB85h+TB85v) [K]

Fig. 1b

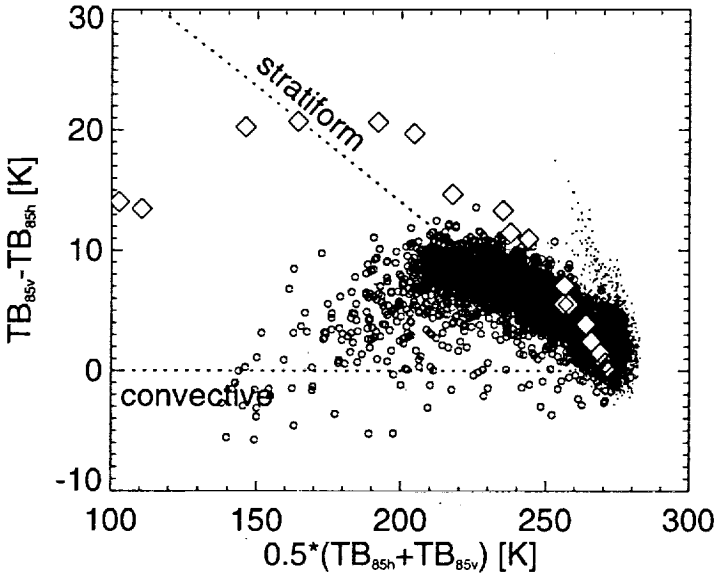
30
20
10
0
-10
100
150
200
250
300
stratiform
convective
TB85v-TB85h [K]
0.5*(TB85h+TB85v) [K]

Figure 2. Texture

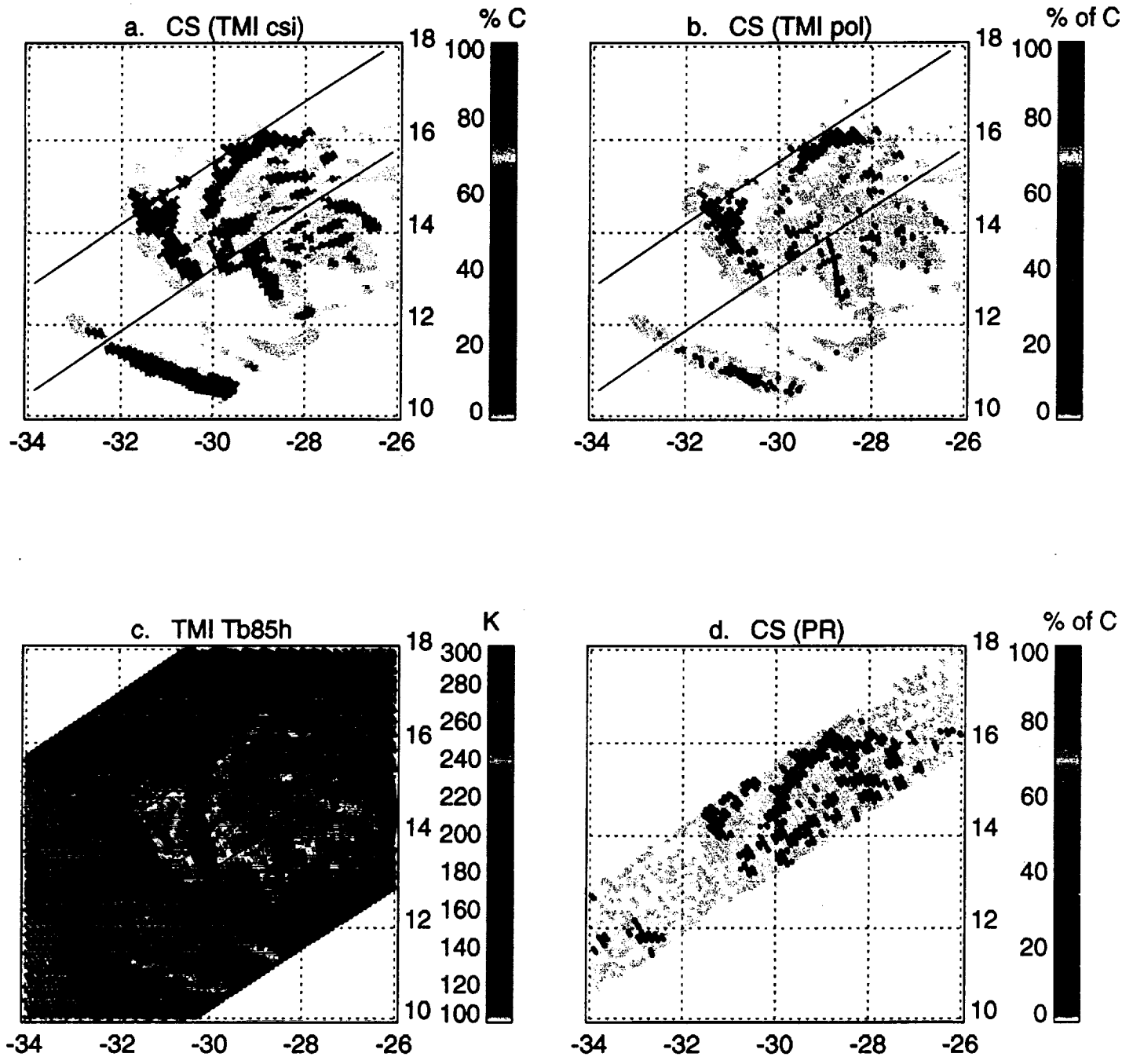

Figure 3. Polarization

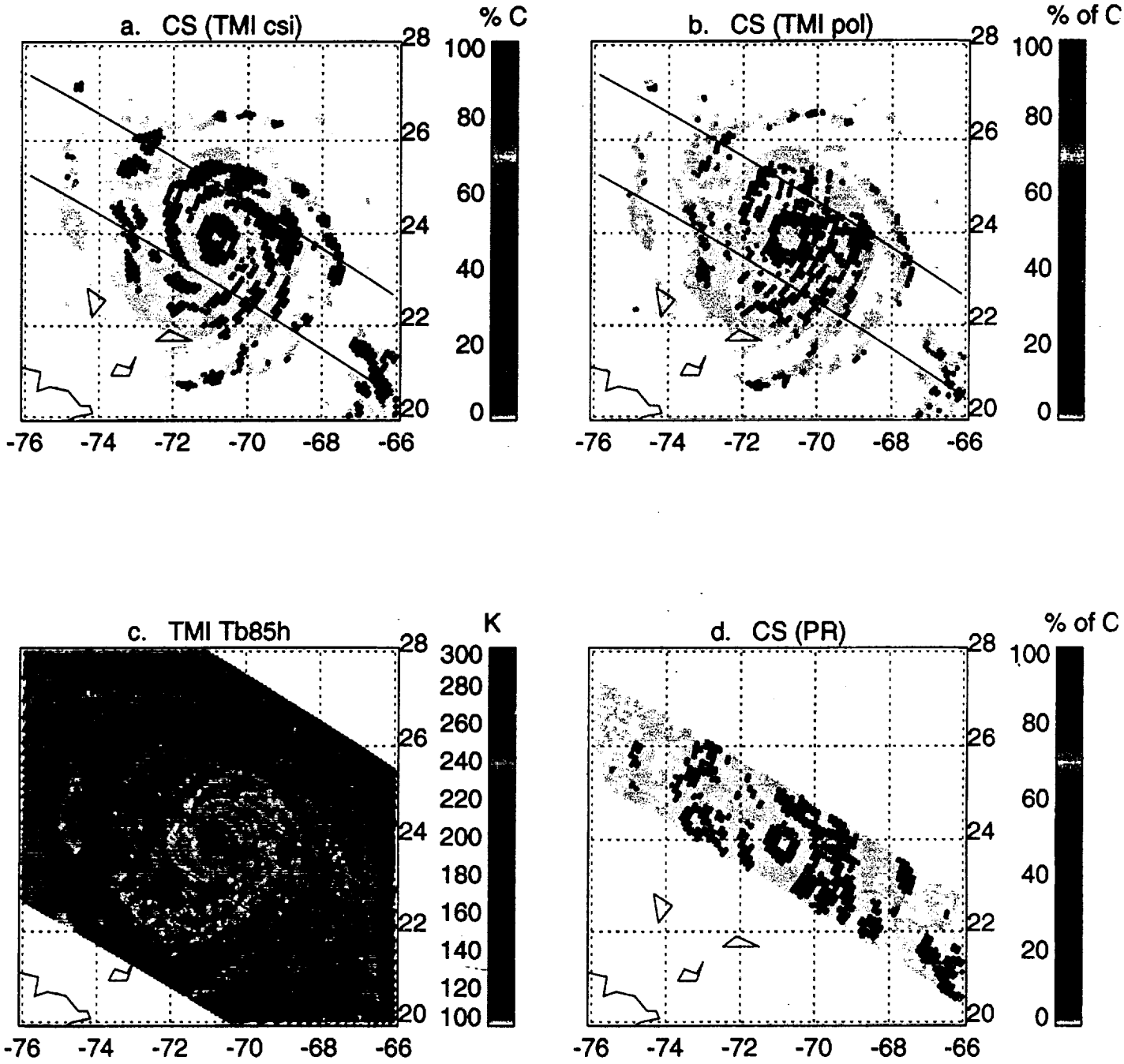

Fig. 4a

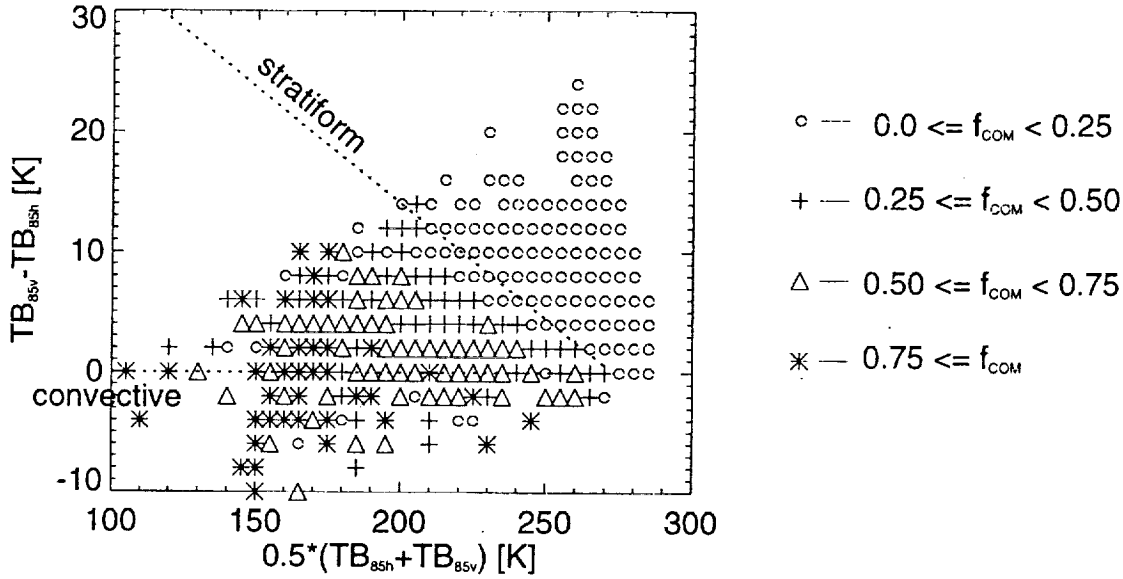
30
20
10
0
-10
100
150
200
250
300
stratiform
convective
TB_{85v}-TB_{85h} [K]
0.5*(TB_{85h}+TB_{85v}) [K]
0.0 <= f_{COM} < 0.25
0.25 <= f_{COM} < 0.50
0.50 <= f_{COM} < 0.75
0.75 <= f_{COM}

Fig. 4b

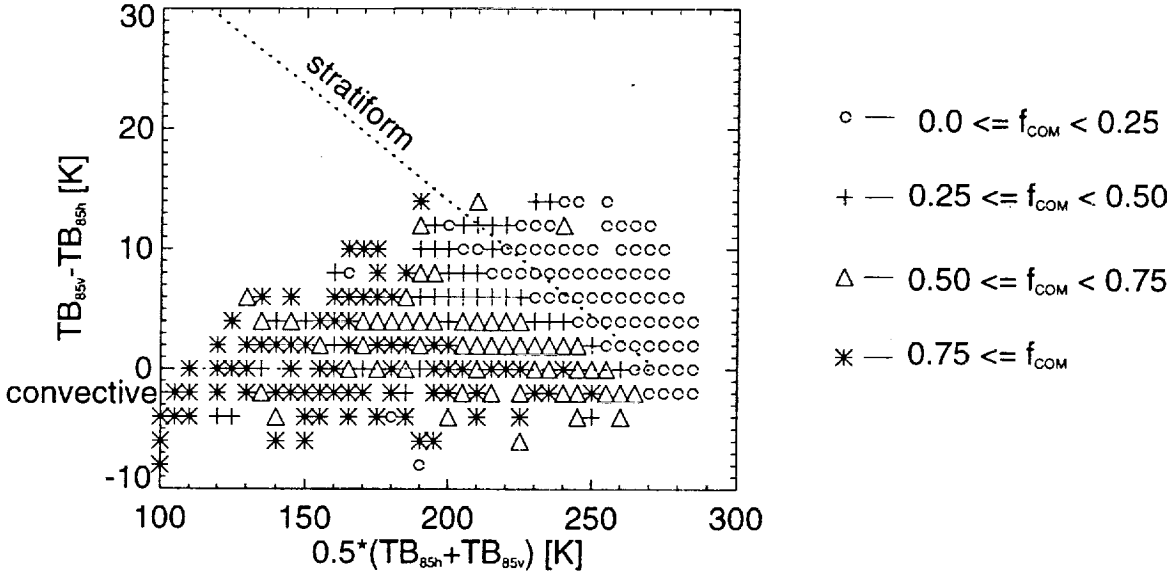
stratiform
convective
30
20
10
0
-10
100
150
200
250
300
TB_{85v}-TB_{85h} [K]
0.5*(TB_{85h}+TB_{85v}) [K]
o — 0.0 <= f_{COM} < 0.25
+ — 0.25 <= f_{COM} < 0.50
Δ — 0.50 <= f_{COM} < 0.75
✳ — 0.75 <= f_{COM}

Figure 5. Ocean cases

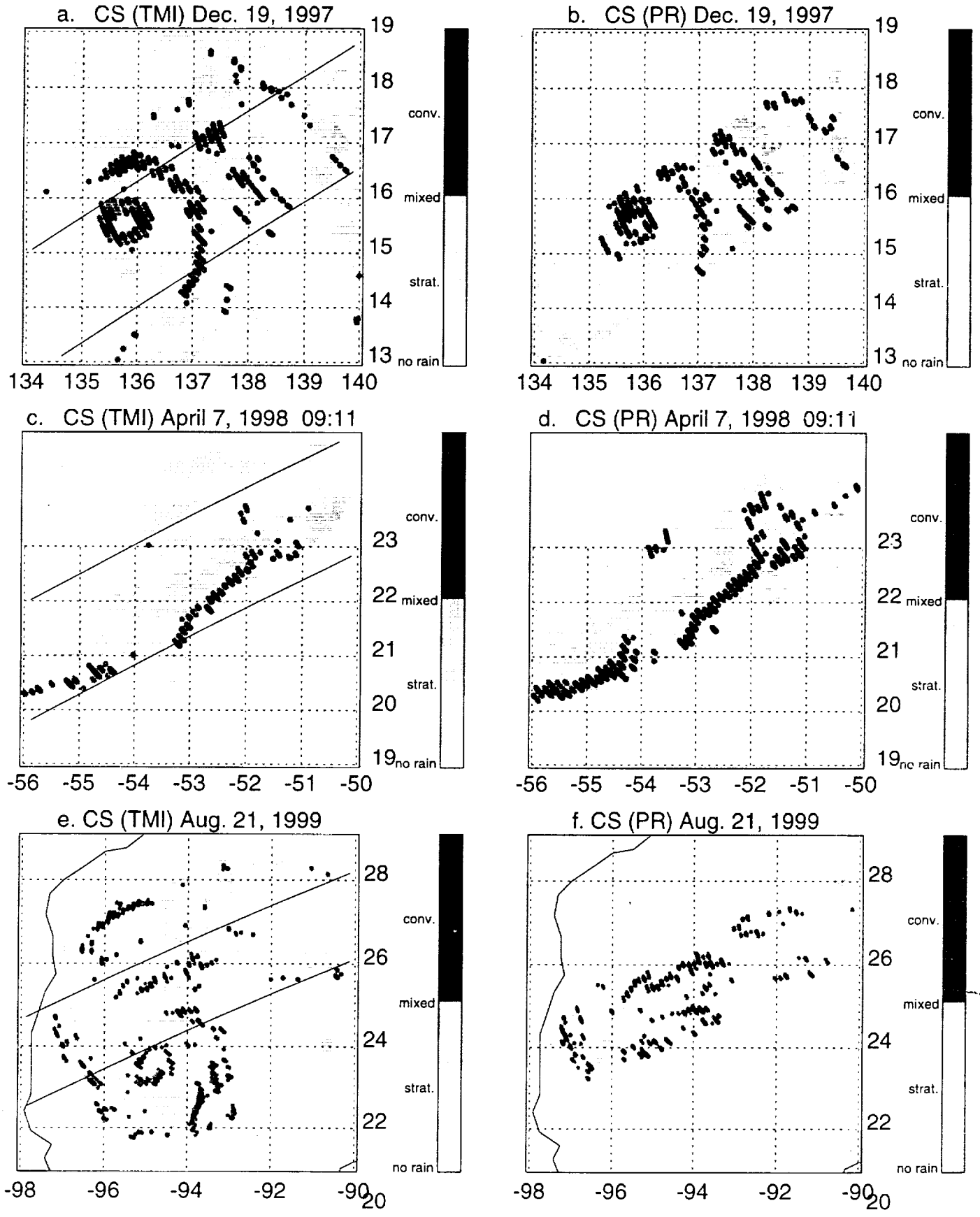

Figure 6. Land cases

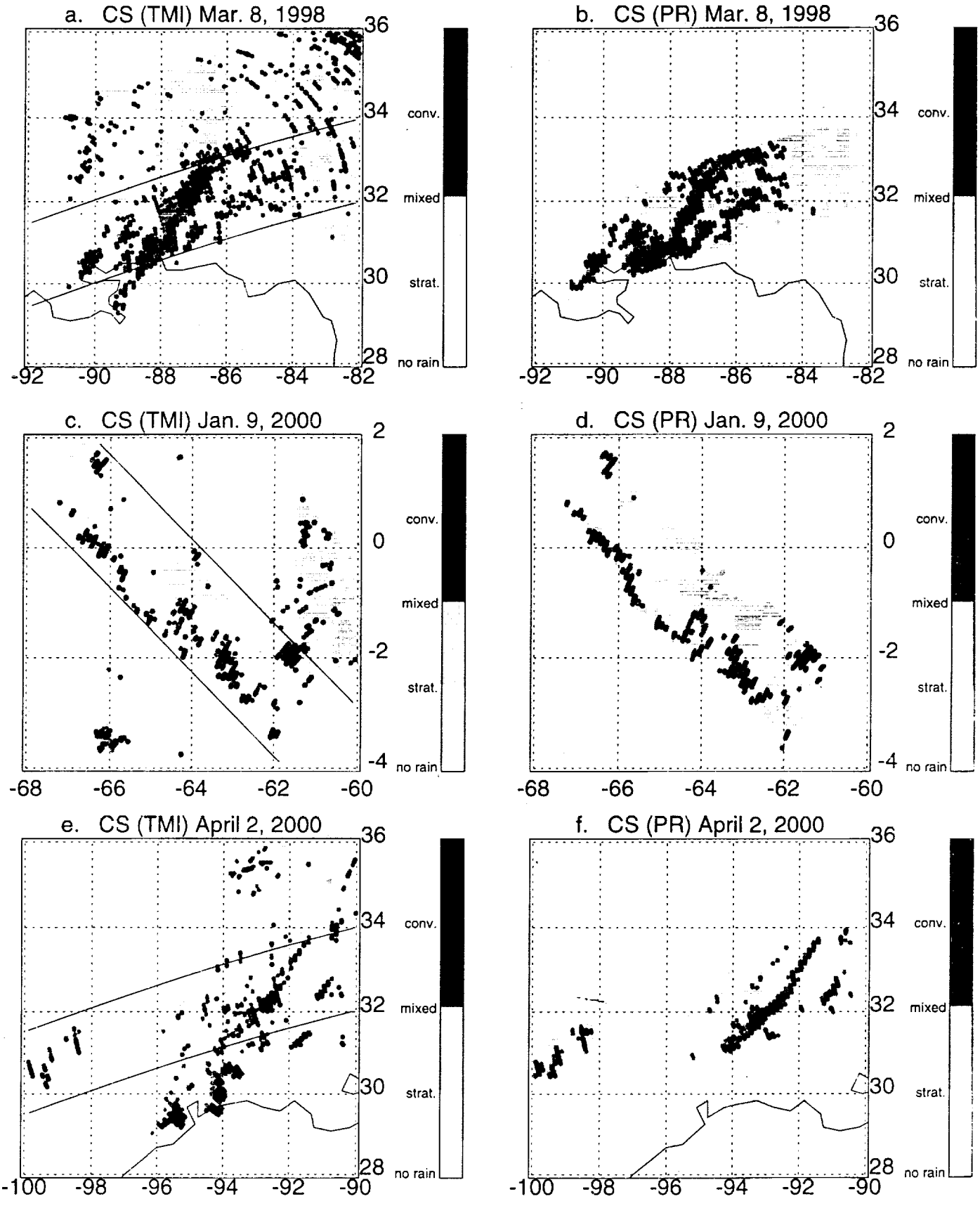

Fig. 7a

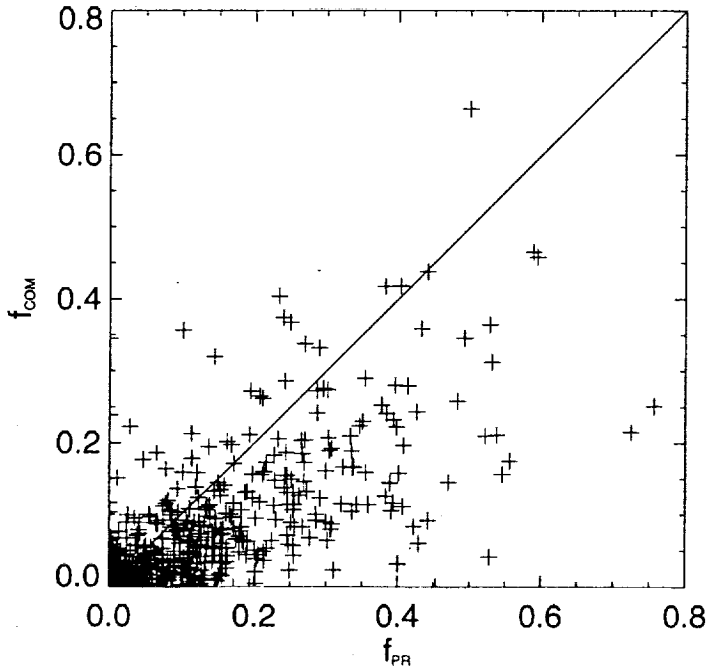

Fig. 7b

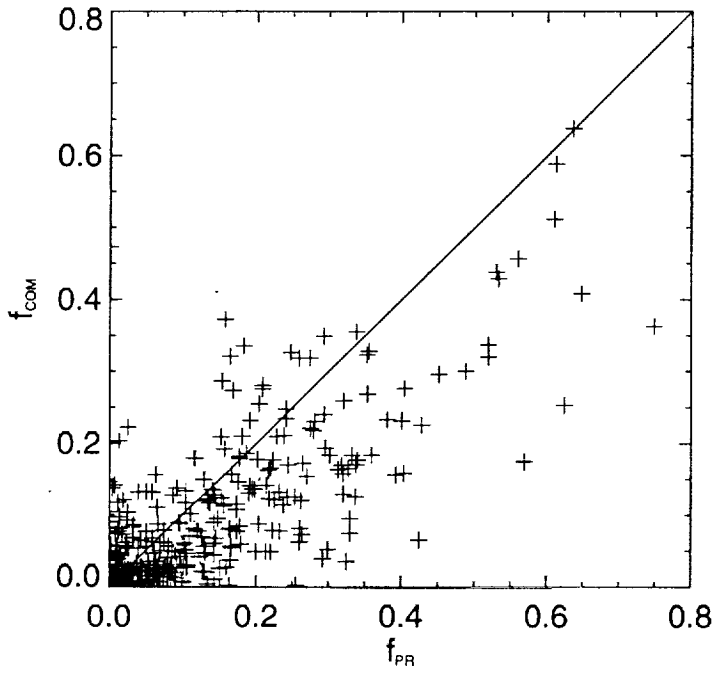

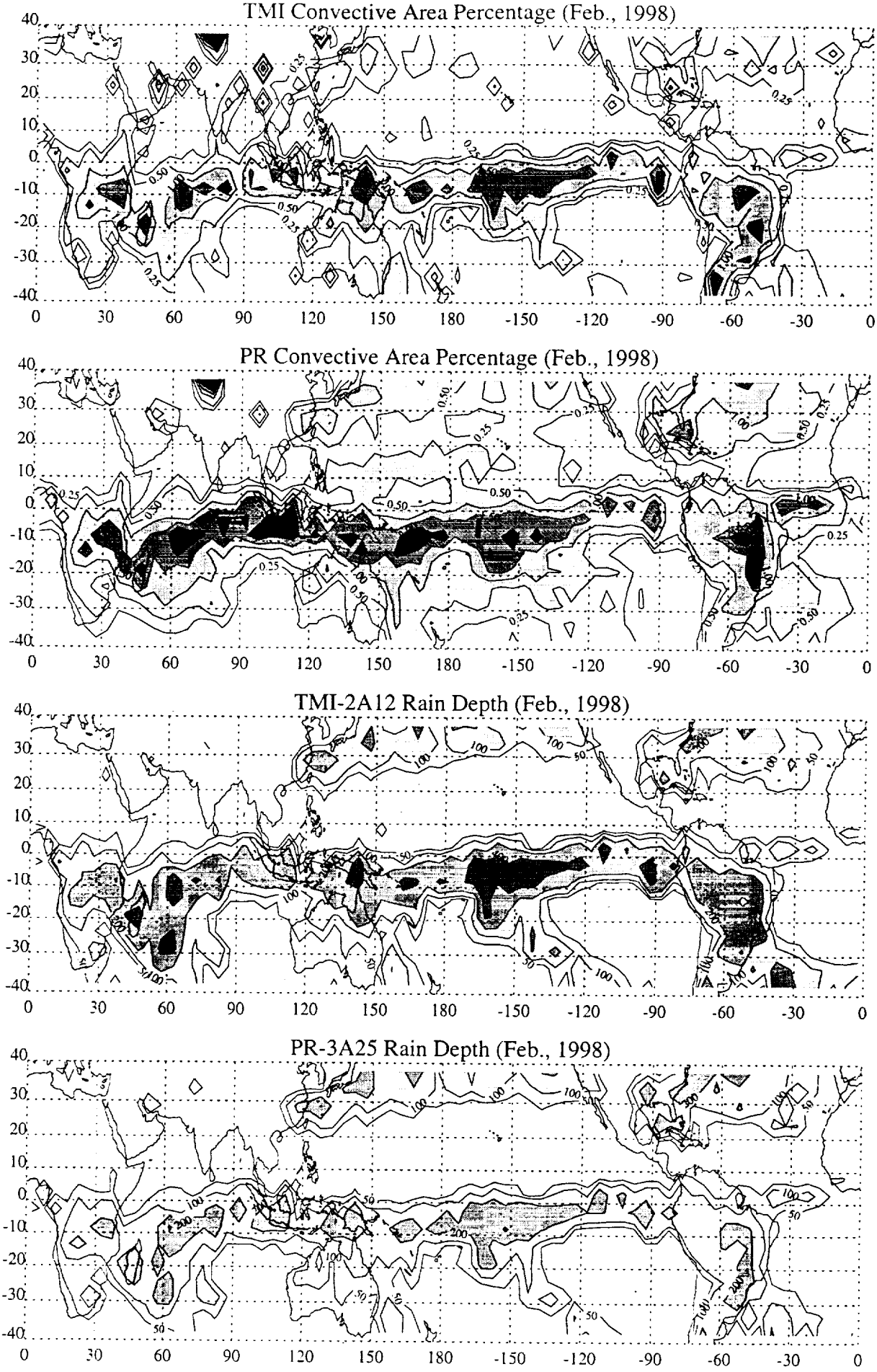
TMI Convective Area Percentage (Feb., 1998)
PR Convective Area Percentage (Feb., 1998)
TMI-2A12 Rain Depth (Feb., 1998)
PR-3A25 Rain Depth (Feb., 1998)
40
30
20
10
0
-10
-20
-30
-40
0
30
60
90
120
150
180
-150
-120
-90
-60
-30
0

Fig. 8

Fig. 9

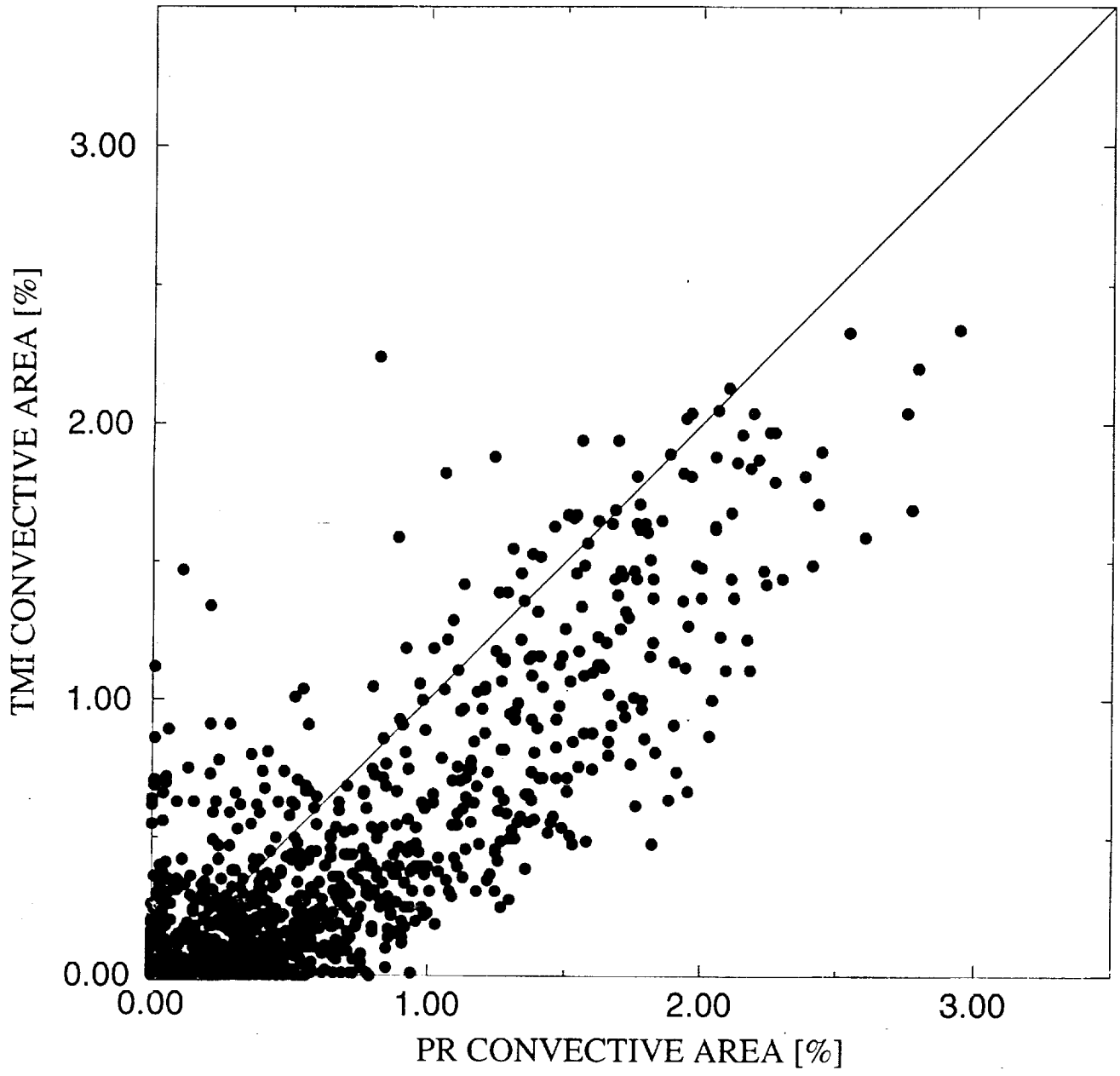
3.00
2.00
1.00
0.00
0.00
1.00
2.00
3.00
TMI CONVECTIVE AREA [%]
PR CONVECTIVE AREA [%]